Graphene Wrapping of Electrospun Nanofibers for Enhanced Electrochemical Sensing

ACS OMEGA

http://pubs.acs.org/journal/acsodf

Article

Graphene Wrapping of Electrospun Nanofibers for Enhanced Electrochemical Sensing

Andreas Tsiamis, Francisco Diaz Sanchez, Niklas Hartikainen, Michael Chung, Srinjoy Mitra, Ying Chin Lim, Huey Ling Tan, and Norbert Radacsi*

Cite This: *ACS Omega* 2021, 6, 10568−10577

Read Online

ACCESS | Metrics & More | Article Recommendations | Supporting Information

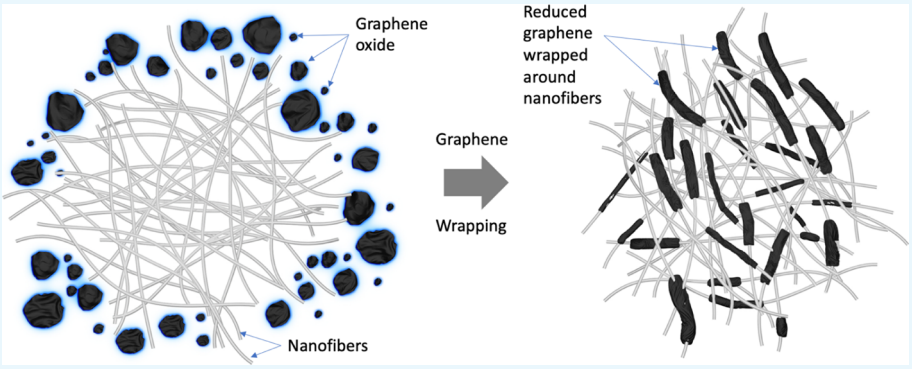

ABSTRACT: This paper presents a scalable method of developing ultrasensitive electrochemical biosensors. This is achieved by maximizing sensor conductivity through graphene wrapping of carbonized electrospun nanofibers. The effectiveness of the graphene wrap was determined visually by scanning electron microscopy and chemically by Fourier transform infrared spectroscopy, Raman spectroscopy, and X-ray diffraction. The sensing performance of different electrode samples was electrochemically characterized using cyclic voltammetry and electrochemical impedance spectroscopy, with the graphene-wrapped carbonized nanofiber electrode showing significantly improved performance. The graphene-wrapped carbonized nanofibers exhibited a relative conductivity of ∼14 times and an electroactive surface area of ∼2 times greater compared to the bare screen-printed carbon electrode despite experiencing inhibitive effects from the carbon glue used to bind the samples to the electrode. The results indicate potential for a highly conductive, inert sensing platform.

1. INTRODUCTION

The development of reliable, robust, ultrasensitive, and low-cost biosensors provides opportunities for point-of-care monitoring of treatment and better disease screening on a large scale. One method of fabricating such sensors is through nanotechnology, offering two fundamental advantages. First, shrinking down to nanoscale dimensions offers logistical improvements: a decrease in the amount of analyte required, a decrease in device size for portability, and a lower cost of mass production, while increasing the detector sensitivity.[1] Second, when approaching single-digit nanometer dimensions, the properties of matter begin to differ significantly with quantum-scale effects playing an important role.[2] By leveraging unique phenomena that only occur at nanoscale dimensions, nanotechnology can be used to design, manipulate, and control the responses and functionalities of different structures or particles.

Currently, there are many potential nanomaterials for medical applications. For example, nanoparticles can be employed for drug delivery to specific types of cells to reduce damage to healthy cells in the body.[3] Functionalized nanorods can be inserted into the bloodstream, providing early disease diagnosis.[1] However, carbon nanofiber (CNF)-based materials are easy to functionalize to extend the CNF-based composite nanomaterials for applications including biosensors,[4] drug delivery,[5] anti-microbial materials,[6] and bone tissue engineering.[7]

One-dimensional CNFs have attracted growing attention particularly in the field of electrochemistry. CNFs exhibit many excellent characteristics such as extremely large surface areas, good electrical conductivity, structural stability, and robust mechanical strength and flexibility,[8] thus making CNFs exceptional candidates for electrode materials and catalyst

Received: November 30, 2020
Accepted: March 16, 2021
Published: April 13, 2021

substrates.[9] Electrospinning offers a facile, low-cost, scalable, and highly controllable technique to synthesize CNFs with tunable nanostructures.[10,11] Although the electrical conductivity of CNFs is relatively high, it is still lower in comparison with those of graphene or carbon nanotubes owing to the incomplete graphitization and the lower specific surface area than graphene and carbon nanotubes.[12] Therefore, it is important to develop porous CNF structures with improved surface areas to further enhance the conductivity of CNFs.

Graphene, on the other hand, is well known for its superior electrical conductivity. It is constructed by a single layer of sp^2 carbon atoms with a hexagonal packed lattice structure.[13] Graphene has advantages over other carbon materials including a high theoretical specific surface area (2630 m^2 g^{-1}) and an excellent intrinsic carrier mobility at room temperature (~10,000 cm^2 V^{-1} s^{-1}).[14] However, irreversible aggregation of graphene sheets as a result of the strong $\pi-\pi$ stacking and van der Waals interaction[15] reduces the large surface area and catalytic effect of graphene. Furthermore, it is very challenging to electrospin polymer solutions incorporated with nanoparticles to achieve an even distribution of the nanoparticles in the fibers. Due to the solution's large specific surface energy, nanoparticles have shown a tendency to aggregate, resulting in an inhomogeneous distribution of nanoparticles in the polymer matrix, or even loss of intended functionality due to the degree of inhomogeneity.[16] The synthesis of graphene-wrapped nanostructures is a novel technique to overcome the problems of agglomeration.[17,18]

In our previous work,[19] we have reported the efficiency of carbonized nanofibers with the inclusion of reduced graphene oxide (rGO) for electrochemical sensing. In the present work, the fabrication of graphene-wrapped carbonized nanofibers with a high surface area and superior electrochemical sensing performance is discussed. The electrospinning technique was adopted for the synthesis of nanofibers using polyacrylonitrile (PAN) and poly(acrylic acid) (PAA). It is anticipated that uniform wrapping of graphene over the CNFs would lead to efficient charge separation across the interface of CNFs/rGO and thus enhance the conductivity. An additional benefit is that the graphene wrap increases the fibers' mechanical stability for its exceptional strength.[20]

2. RESULTS AND DISCUSSION

2.1. Fiber Morphology. To determine the effectiveness of the electrospinning process, the shape, morphology, size, and thus quality of the electrospun PAN/PAA nanofibers were investigated by scanning electron microscopy (SEM) imaging. Figure 1a shows a typical imaged section of the fibers. The as-spun fibers were abundant with a smooth surface and randomly oriented. Fiber thickness measurements on a number of arbitrarily selected fibers confirmed nanometer dimensions ranging from 275 to 625 nm. Additionally, SEM images were obtained to visually assess the effectiveness of graphene wrapping electrospun and carbonized PAN/PAA nanofibers. It can be clearly observed that after the graphene wrapping process, the smooth surface of PAN/PAA nanofibers becomes wrinkled and rough, as evident in Figure 1b,c. A faint layer of rGO encapsulating the fibers is visible from the gray-scale image contrasts. In Figure 1c, the fibers resemble a "yarn" of fibers. This yarn-like morphology is likely a consequence of the constant magnetic stirring occurring during the graphene wrapping procedure. For some sections of the sample where the fiber density was high, the graphene wrap manifested itself

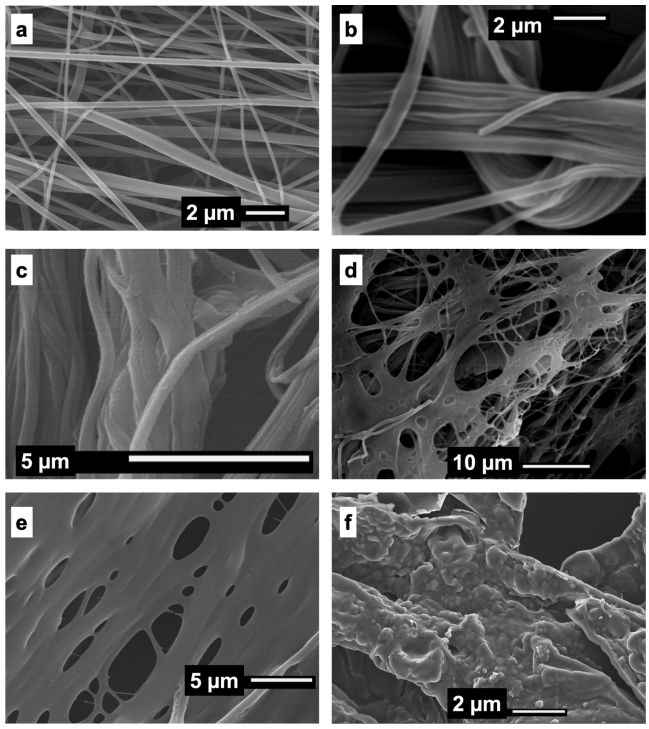

Figure 1. SEM images of (a) typical electrospun PAN/PAA nanofibers and (b–f) the graphene wrapping process. (b) Faint layers of rGO encapsulating fibers. (c) An example of a graphene-wrapped "yarn" of fibers, which is most likely a consequence of the constant stirring required in the graphene wrapping method. (d) The graphene wrap is agglomerated as sheets instead of encapsulating individual fibers in areas of a high fiber density. (e) Smooth nanofiber morphology after carbonization. (f) Surface texture of the graphene-wrapped carbonized nanofibers.

in the form of agglomerated sheets instead of wrapped fibers, as seen in Figure 1d.

The carbonized nanofibers shrunk during the stabilization and carbonization processes as water and solvents evaporated from the fibers. The degree of weight loss is presented in Table 1. It should be noted that weight loss experiments are difficult

Table 1. Weight Loss Experienced by the Electrospun Nanofibers during the Stabilization and Carbonization Processes

	before stabilization	after stabilization	after carbonization
fiber weight (milligrams)	68.8	63.9	25.9
percentage of the original weight	100%	92.9%	37.6%

to reproduce with small experimental errors and the results reported in this paper are from the measurement of a single sample. Therefore, they represent an initial indication for the degree of weight loss due to stabilization and carbonization. During carbonization, the well-defined fibers are grouped to create less defined but smooth, fiber-like structures, as seen in Figure 1e. After graphene wrapping, the carbonized fibers showed a rough, rugged surface texture, indicating that a layer of graphene was deposited onto the carbonized fibers (Figure 1f).

Finally, focus ion beam-SEM (FIB-SEM) was used to further evaluate the effectiveness of the graphene wrap by milling the

https://doi.org/10.1021/acsomega.0c05823
ACS Omega 2021, 6, 10568−10577

fibers and then inspecting their cross-sections. The images presented in Figures 2 and S2 further suggest that the graphene

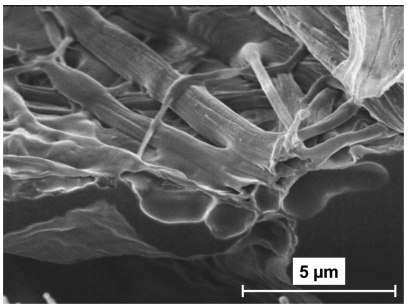

Figure 2. FIB-SEM imaging of the graphene wrapping process. The graphene structures appear to be hollow since no polymer fibers can be seen. The polymer fibers could have melted from the high energy of the ion beam.

wrapping method was successful. However, the rGO structures appear to be hollow. This could be attributed to the focused ion beam milling of the sample with energy high enough to melt the polymer fibers, coupled with the fact that polymers have low melting points. rGO would not naturally create hollow structures, implying that there must have been nanofibers inside them during the creation of the structures. Additionally, the images suggest that the graphene wrapping process is uniform and continuous.

2.2. Fourier Transform Infrared Spectroscopy. Figure 3 presents the Fourier transform infrared (FTIR) spectra for the nanofibers, which were wrapped in graphene after electrospinning. As the layer of the graphene wrap is only around 5 nm thick, the contributions from the underlying polymer backbones of the fibers should also be visible in the FTIR spectrum.[20] The presence of the characteristic peaks at 2950−2850, 2239, 1716, 1226, and 1254 cm^{-1} is attributed to the C−H, C≡N, C═O, C−OH, and C−C stretching vibrations of the PAN/PAA polymer blend, respectively, implying that the underlying polymer backbone was synthesized successfully through electrospinning.[21] More importantly, the presence of C═C (1450 cm^{-1}) and C−O (1060 cm^{-1}) bonds suggests a successful graphene wrap[22] as these bonds do not normally appear in the spectrum for untreated fibers.

2.3. X-ray Diffraction. The GW and GW + CB samples were characterized by X-ray diffraction (XRD) over an angle range of 5−50°, in which a visible peak can be expected. Figure 4 shows the obtained XRD patterns. Both spectra appear very similar, with both samples showing a diffraction peak at an angle just above 25°. This is in accordance with the expected rGO peak at 25.5° (JCPDS no. 01-0646).[23] Therefore, XRD analysis suggests that the samples are wrapped in rGO.

The intensities of the rGO peaks in the spectrums are 2295 and 1724 counts for the GW + CB and CB samples, respectively. This noticeable difference is indicative of the quality of the graphene wrap. The graphene wrap appears to have adhered better to the chemical structure of the carbonized fibers than to the untreated fibers. These chemical characterization results provide further evidence for the success of the graphene wrapping method.

2.4. Raman Spectroscopy. From the obtained base-lined and smoothed spectrum presented in Figure 5, three peaks can be observed: two strong peaks at 1325 and 1602 cm^{-1} and one weak broad peak at 2628 cm^{-1}. These correspond to the so-called D, G, and 2D peaks, respectively, and are characteristic of sp^2-hybridized carbon materials.[24] The D peak relates to the disorder and defects in the structure of the carbon system, while the G peak arises due to C−C bond stretching. An intense 2D peak is commonly seen in graphene materials and typically reduces in intensity as the number of layers of graphene increases. In this Raman spectrum, the 2D peak is very weak compared to the D and G peaks. This low 2D peak intensity might suggest the presence of a large number of defects in the structure and probably a large amount of lattice distortion. This can cause a reduction in the intensity of the defect-sensitive 2D peak.[25] Further, the reduction level of graphene oxide (GO) might be low.

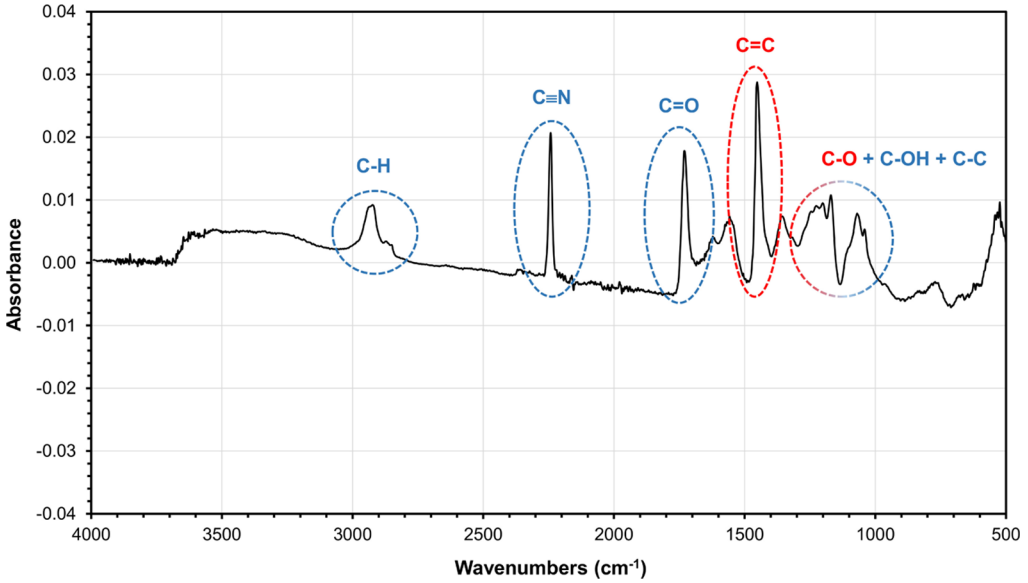

Figure 3. Annotated FTIR spectrum of the graphene-wrapped electrospun nanofibers. The presence of C−H, C≡N, C═O, C═C, C−OH, C−C, and C−O bonds can be identified. The C═C and C−O bonds (red) are attributable to the graphene wrap, while the rest (blue) are attributable to the PAN and PAA polymers of the nanofibers.

https://doi.org/10.1021/acsomega.0c05823
ACS Omega 2021, 6, 10568−10577

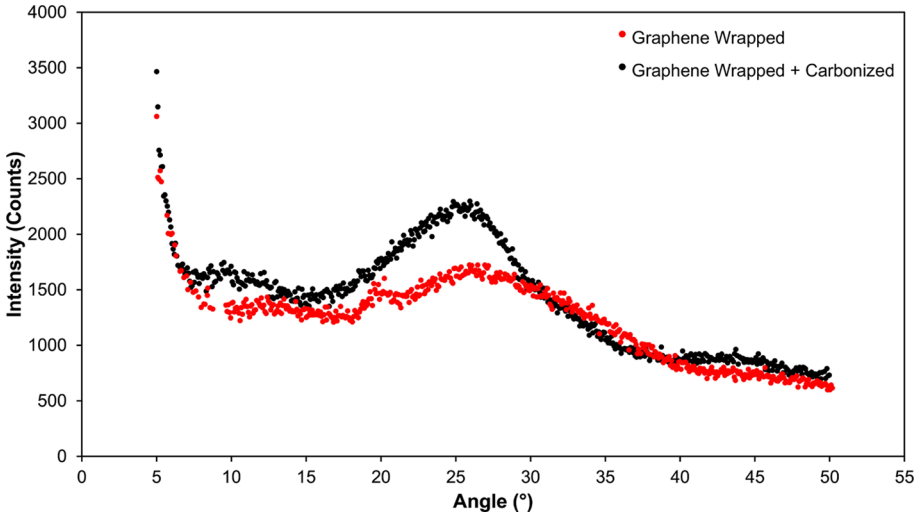

Figure 4. XRD spectra of the graphene-wrapped (red) and graphene-wrapped + carbonized (black) nanofibers.

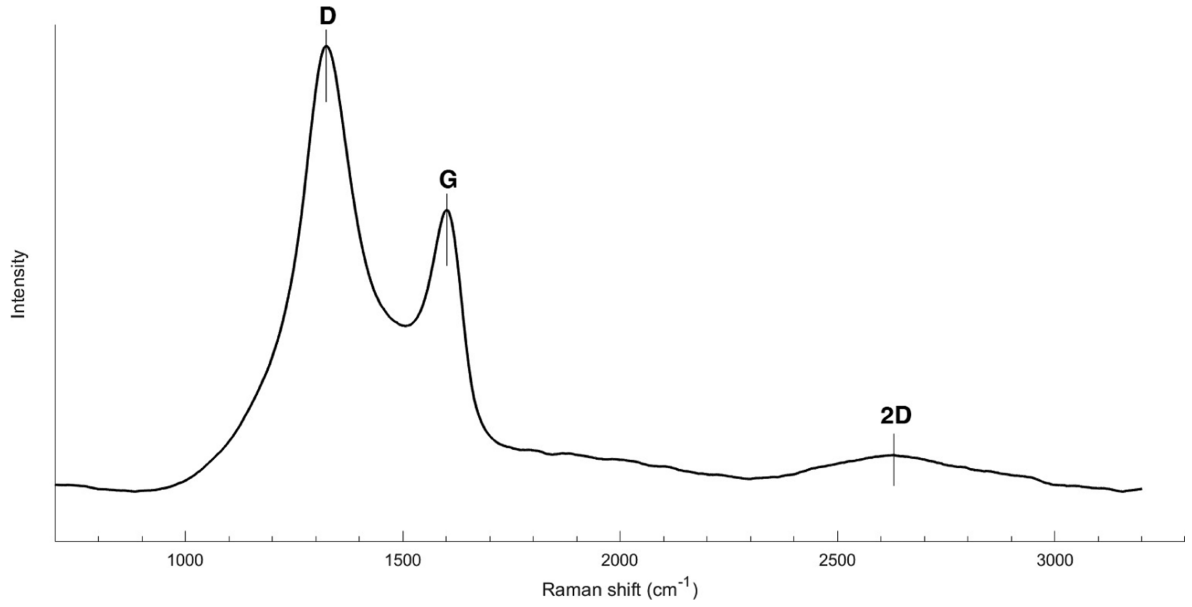

Figure 5. Raman spectrum of rGO-wrapped PAN/PAA electrospun fibers.

One key point to consider for this Raman data is that even if the original GO system is dominated by fully disordered sp^2 bonds, upon successful reduction to rGO, a change should be observed in the 2D peak with an increase in intensity and a potential splitting of the 2500−3000 cm^{-1} region into multiple peaks.[26,27] Since the 2D peak is not intense enough to be clearly defined in the current spectrum, the data suggest that the GO present in the analyzed sample was not fully reduced. This would lead to poor electrical conductivity of the graphene in the material.

2.5. Electrochemical Measurements. *2.5.1. Cyclic Voltammetry.* In the electrochemistry process, cyclic voltammetry (CV) is an important analytical technique used to determine the nature of electrode reactions. To compare the electrochemical performances of all the fabricated electrodes, CV measurements were made with 2 and 10 mM $K_4Fe(CN)_6$ solutions, setting the scan rates as 0.02, 0.04, 0.06, 0.08, 0.1, and 0.2 V s^{-1}. While typical CV curves for the bare electrode and solution used for these experiments are expected to show clear redox peaks and would resemble the characteristic duck-shaped curve often referenced as the standard response for CV, the response curves observed for all the modified electrodes showed varying degrees of deviation from the response.

The redox current responses of the different electrode samples in $K_4Fe(CN)_6$ show reversible redox reactions with well-defined oxidation and reduction peaks at 2 mM $K_4Fe(CN)_6$ solution concentrations, as presented in Figure 6. In the case of a screen-printed carbon electrode (SPCE) modified with conductive carbon glue, the lack of defined peaks in the CV curve indicates that the electron-transfer kinetics was rather slow during the redox reactions of $[Fe(CN)_6]^{3-/4-}$ in comparison with the unmodified bare SPCE which is used as the reference (control sample). The glue layer appears to have an inhibitive effect on the redox reaction, therefore distorting the shape of the curve. This effect is ascribed to carbon glue being a medium with relatively low conductivity. In this study, carbon glue was used as the binding agent between the various nanofiber samples and the SPCEs; thus, all the fabricated electrodes will experience the same inhibitive effect. SPCE with carbonized nanofibers demon-

https://doi.org/10.1021/acsomega.0c05823
ACS Omega 2021, 6, 10568−10577

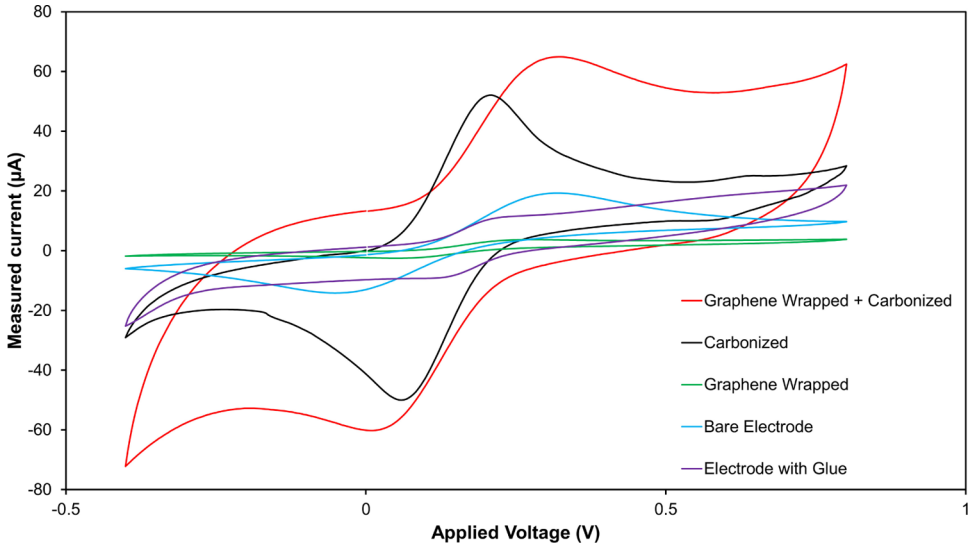

Figure 6. Cyclic voltammograms (0.04 V s^{-1} scan rate) of the five electrode samples tested: bare (blue), glue (purple), graphene-wrapped (green), carbonized (black), and graphene-wrapped and carbonized (red) in 2 mM $K_4Fe(CN)_6$. SPCE fabricated with graphene-wrapped carbonized nanofibers exhibited the highest current redox response, showing the significance of carbonization and graphene wrapping in increasing the electron-transfer kinetics.

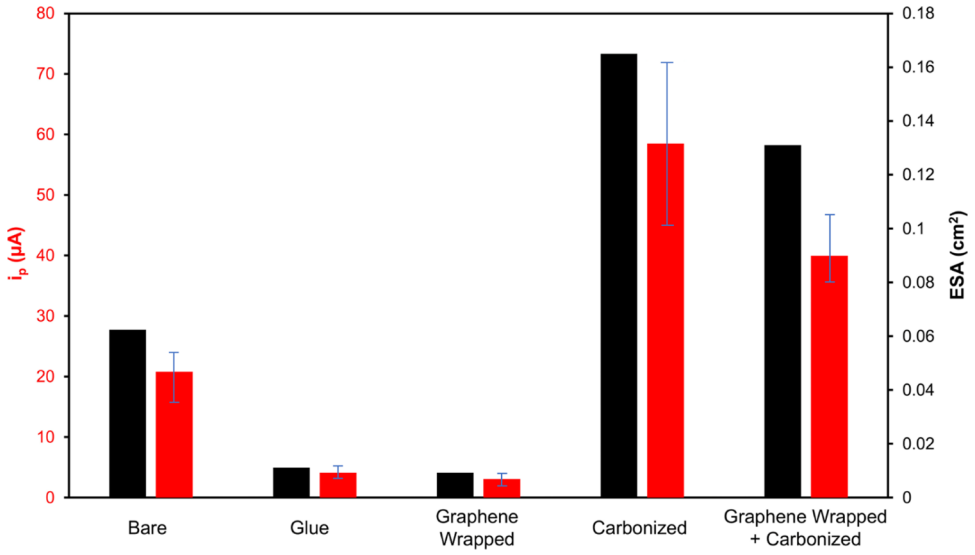

Figure 7. Peak currents and ESAs of the five electrode samples tested: bare, glue, graphene-wrapped, carbonized, graphene-wrapped, and carbonized.

strated enhanced performance, indicating that the carbonized nanofibers are able to compensate for and moreover increase the redox reactivity of the electrode despite the inhibitive effects from the conductive glue.

Surprisingly, SPCE fabricated with GW non-carbonized nanofibers showed a very weak current. While SEM imaging suggested that uniform graphene wrapping had been achieved, the recorded current readings suggest that the GW coverage has discontinuities. Besides offering a higher degree of mechanical stability for the PAN/PAA nanostructures, another critical role of graphene was to enhance the conductivity of the electrode. The combined GW PAN/PAA structures would ideally provide low loss media, coupling a transition from the monolithic carbon electrode surface of the electrode into a high surface-area network of fibers. From observing the response curve of the GW sample, it is safe to assume that the GW method does not result in perfect coverage, likely due to the presence of several breaks and fissures along with the wrapping. Given that the electrospun PAN/PAA nanofibers are poor electrical conductors, the presence of fissures and breaks in the GW surfaces explains why the current on the GW electrode is weak. However, for the GW + CB electrode, the fibers are much more conductive due to their high carbon content and therefore are able to transmit the current past points of discontinuities with more ease. As seen in Figure 6, the GW + CB electrode experienced a higher current level than the CB electrode. However, the measurements at a 10 mM solution concentration showed significant deviations in the redox reactions and a slightly lower current than was measured with the carbonized electrodes (see Figure S3 in Supporting Information). These observations indicate that the graphene wrap does increase conductivity under certain conditions despite being discontinuous and that the electrode conductivity is also dependent on the material being graphene-

https://doi.org/10.1021/acsomega.0c05823
ACS Omega 2021, 6, 10568−10577

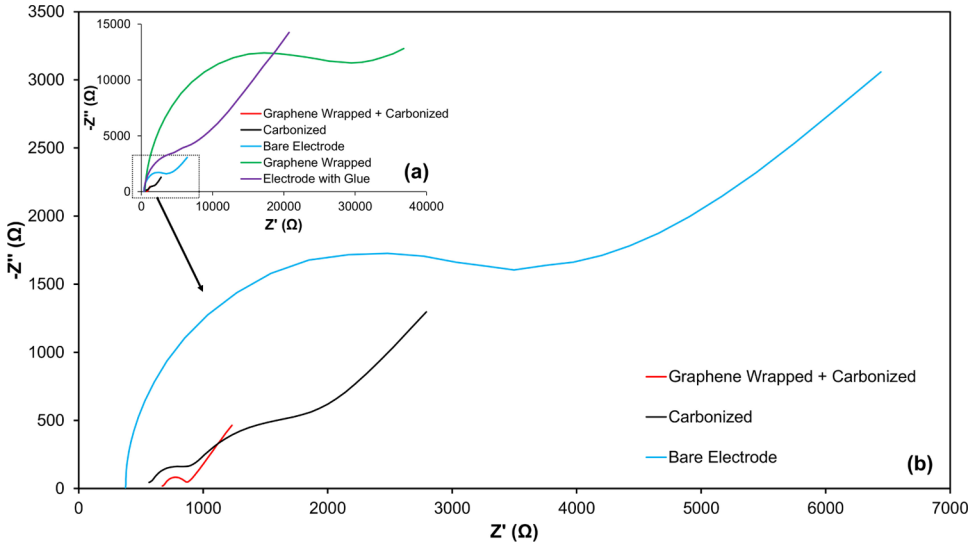

Figure 8. EIS Nyquist plots (frequency range 100 kHz to 1 Hz) for the (a) five different electrodes tested and (b) blown-up spectra for the bare, CB, and GW + CB electrodes.

wrapped. This is in agreement with the observations from XRD analysis.

Once the peak currents for each electrode are extracted, the Randles–Sevcik equation (eq 1) can be used to solve for the electroactive surface area (ESA) of the effective electrodes

$$i_p = 0.4463\, nFAC\left(\frac{nFvD}{RT}\right)^{1/2} \quad (1)$$

where i_p = peak current (A), n = number of electrons transferred in the redox reactions, F = Faraday constant (C mol^{-1}), A = electrode area (cm^2), C = concentration (mol cm^{-3}), v = scan rate (V s^{-1}), D = diffusion coefficient (cm^2 s^{-1}), R = gas constant (J K^{-1} mol^{-1}), and T = temperature (K).

By approximating the room temperature to be 25 °C (298 K), the Randles–Sevcik equation can be simplified to eq 2

$$i_p = 268,\ 600n^{3/2}AD^{1/2}Cv^{1/2} \quad (2)$$

The peak currents (measured as triplicates) and ESAs of the different electrode samples are presented in Figure 7.

It can be seen that the GW + CB and CB electrodes have larger ESAs than the bare electrode. The CB electrode exhibited the largest ESAs and the highest current levels. This could be explained by the carbonized nanofibers having the highest compatibility with the carbon SPCE surface. The carbon working electrode (WE) of the SPCE and the high carbon content of the carbonized nanofibers are structurally the most similar and matched. Any interfacing of materials results in some loss of function. Matching two very similar materials together minimizes this functional loss. Additionally, the glue electrode has the lowest current levels. This confirms that carbon glue has an inhibitive effect on the redox reactions.

Based on the CV analysis, the CB and GW + CB electrodes appear to be the best candidates for sensing applications. They both significantly exceeded the bare electrode ESA despite experiencing the inhibitive effect of carbon glue. The CB and GW + CB electrodes had ESAs of 2.64 and 2.10 times that of the bare electrode, respectively.

2.5.2. Electrochemical Impedance Spectroscopy. Electrochemical impedance spectroscopy (EIS) characterization was performed to evaluate the kinetic process of bare SPCE, bare glue, CB, GW, and the CB + GW electrode in 2 mM $K_4Fe(CN)_6$ solution, and the obtained EIS Nyquist plots for all five types of electrodes are shown in Figure 8a. The bare electrode plot resembles the typical shape associated with the Randles cell model, implying that the behavior of the bare electrode in the established testing conditions points to having the reaction being controlled by both the reaction kinetics at the surface of the electrode and diffusion that takes place between the depleted microenvironment surrounding the electrode and the bulk solution used in the experiment, with the predominance of the effects being dependent on the frequency of the signal being applied to the cell. Taking the curve for the bare electrode as a basis for electrode behavior under an applied family of small AC signals of various frequencies, the GW + CB electrode and the CB electrode have lower impedance figures. These curves are shown in red and black, respectively, in Figure 8b.

These findings suggest that these two samples effectively reduced the impedance of the electrode, possibly by having increased the effective area exposed to the electrolyte. These results are in agreement with the CV measurements, where GW + CB and CB had the highest current levels in addition to being the only electrodes capable of exceeding the bare electrode ESA.

An estimate of relative electrode conductivities can be obtained by calculating the reciprocals of their semicircle diameters. It is reported that a smaller diameter of the semicircle in the high-frequency region of a Nyquist plot suggests faster electrode reaction kinetics. The semicircular regions of the GW + CB and CB electrode EIS curves have diameters of 153.21 and 281.87 Ω, respectively, indicating that the electrochemical reaction rate was faster on the surface of the GW + CB electrode where it has a conductivity of ∼1.84 times higher than that of the CB electrode. Additionally, the GW + CB electrode has a capacitive fit of 0.85 compared to the CB electrode's 0.79. The capacitive fit is a semicircular line of regression, represented by a number between 0 and 1. It describes how well the regression fits the experimental data points obtained, with a value of 1 being a perfect fit. The capacitive fit indicates how close the double-layer charging that occurs on the surface of the electrode approaches the behavior

https://doi.org/10.1021/acsomega.0c05823
ACS Omega 2021, 6, 10568−10577

of an ideal capacitor. Changes in surface geometry and composition of the electrode affect the reaction kinetics occurring on the system, which in turn results in lower values for the capacitive fit.[28] Having an electrode with almost ideal properties is particularly desirable for a biosensor to prevent electrode interference with biological processes such as the activity of immobilized enzymes. The GW + CB electrode has both a higher conductivity and a higher capacitive fit compared to the CB electrode, making it the best candidate for a biosensor electrode material.

The shape of the EIS curve for the CB electrode appears to display second-order behavior, with the formation of a second semicircular region. This suggests that an unknown effect influences the curve. For comparison purposes, the first-order fit is used and the CB electrode is assumed to be compatible with the Randles model.

As the GW + CB electrode showed a higher conductivity and capacitive fit than the CB electrode, it is then compared with the bare electrode to observe the degree of enhancement it provides on the SPCE's sensing performance. The GW + CB electrode is calculated to have a conductivity 14.36 times higher than that of the bare electrode (a semicircle diameter of 2200 Ω). The capacitive fit of 0.85 is lower than that of the bare electrode (0.96) due to the introduction of interfacing but is still the higher fit-out of the GW + CB and CB electrode samples. It should be noted that the GW + CB electrode was attached to the SPCE using carbon glue, which according to the CV measurements has detrimental effects on the electrode in the form of redox reaction inhibition and ESA reduction. Nevertheless, it was able to improve the redox current response and exhibited a 210% increment of the ESA when compared with the bare electrode. Therefore, based on the electrochemical characterization, the GW + CB electrode shows promising potential in sensing applications. Despite the hindrance of carbon glue, the GW + CB electrode was able to significantly outperform the bare electrode.

3. CONCLUSIONS

This paper presented the development of an efficient electrochemical sensing nanomaterial, fabricated from electrospun PAN/PAA nanofibers. The electrospun nanofibers were modified through the processes of carbonization and graphene wrapping in an attempt to maximize their conductivity. The success of the graphene wrap was characterized by imaging, chemically, and electrochemically. SEM and FIB-SEM suggested that the graphene wrapping had been successful and that it was continuous along the fibers. Chemically, FTIR and XRD confirmed that the graphene coating was in fact rGO and that rGO adhered better to carbonized nanofibers than their untreated counterparts. However, Raman spectroscopy indicates that the reduction level of GO is low. Electrochemical results suggest that either the reduction of non-conducting GO to highly conductive rGO was low or the graphene wrapping was discontinuous. Nevertheless, the graphene-wrapped and carbonized electrode outperformed the other electrode samples in CV and EIS. The graphene-wrapped and carbonized electrode exhibited a relative conductivity of 14.36 times and an ESA of 2.10 times greater than those of the bare screen-printed electrode despite experiencing inhibitive effects from carbon glue. The graphene-wrapped and carbonized electrode also obtained a capacitive fit of 0.85, the highest of any of the interfaced electrode samples tested, suggesting that it would provide a biosensor platform with behavior closely resembling that of the Randles model.

4. MATERIALS AND METHODS

4.1. Materials. Polymers, PAN (Shandong Jianuofu Treasure Industrial Co.) and PAA (Sigma-Aldrich) with weight-average molecular weights (M_W) of 150,000 and 450,000 g·mol^{-1}, respectively, were used for preparing the precursor solutions. The polymer−solvent used was *N*,*N*-dimethylformamide (DMF), 99% pure (Alfa Aesar). Toluene (Fisher Scientific); 3-aminopropyltriethoxysilane (APS), 99% pure (ACROS Organics); hydrochloric acid (HCl) (Sigma-Aldrich); hydrazine monohydrate (Fisher Scientific, diluted in water to 50%); and aqueous GO were used for the graphene wrapping process. Potassium hexacyanoferrate(II) [$K_4Fe(CN)_6$] (Sigma-Aldrich), sodium phosphate buffer (PBS), and potassium chloride (KCl) (extra pure, ACROS Organics) were used for the electrochemical characterization. Three-electrode SPCEs (Metrohm Dropsens, DRP C110) comprising a 4 mm diameter circle WE, a counter electrode, and a Ag reference electrode were used for attaching the nanofibers to the WE, with conductive carbon glue (Pelco).

4.2. Electrospinning Solutions and Apparatus. The precursor solutions were prepared by dissolving PAN (12 wt %) or PAA (12 wt %) in DMF. The PAN solution was stirred (700 rpm) at 80 °C for 3 h, while the PAA solution was stirred (700 rpm) overnight at 150 °C. The two prepared solutions were mixed at a 7:1 PAN/PAA w/w ratio and stirred at 180 °C for 15−20 min to prepare the master solution for electrospinning.

The homebuilt nozzle-free electrospinning setup consisted of a motorized rotating solid stainless-steel electrode (electrospinning electrode) rotating at 5 rpm inside a Teflon bath, where the PAN/PAA solution was poured, and a rotating aluminum collector (collector electrode, rotating at 500 rpm). The working distance between the electrospinning electrode and the collector electrode was 150 mm. A potential difference of 60 kV DC was applied between the two rotating electrodes (+30 kV on the electrospinning electrode inside the Teflon bath and −30 kV on the collector electrode). Aluminum foil was used to collect the fibers. All electrospinning was carried out under ambient conditions at a humidity level of 20%, which was reached by introducing nitrogen gas into the chamber. Figure 9 shows a schematic layout of the used nozzle-free electrospinning setup with the applied process parameters.

4.3. Stabilization and Carbonization Process and Apparatus. Both stabilization and carbonization processes were performed using a horizontal tube furnace with metal

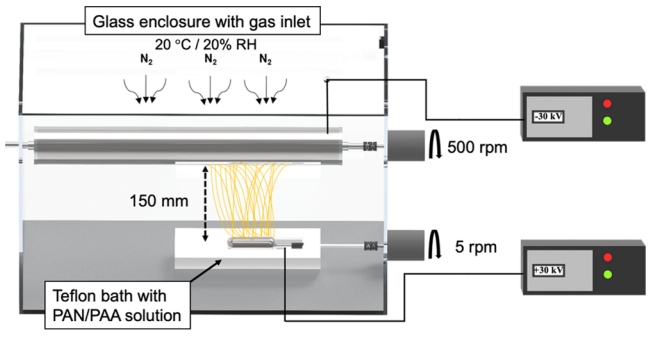

Figure 9. Schematics of the nozzle-free electrospinning setup.

https://doi.org/10.1021/acsomega.0c05823
ACS Omega 2021, 6, 10568−10577

seals (OTF-1200X, MTI Corporation, an ∼2 in. outer diameter, an ∼510 mm length quartz tube, the Fe−Cr−Al alloy doped by the Mo heating element) and with control over temperature, time, heating/cooling rates, and the gas atmosphere. The electrospun PAN/PAA precursor nanofibers were inserted into the reaction zone of the tube furnace, and stabilization was performed at 200 °C with a heating rate of 10 °C min^{-1} using an airflow rate of 70 mL min^{-1}. The samples were then maintained at the final temperature for 30 min. The samples were cooled and weighed. Prior to the carbonization process, the tube of the furnace was purged with nitrogen gas for 15 min to remove any O_2. The stabilized samples were heated from room temperature to 750 °C, with a heating rate of 10 °C min^{-1} using N_2 (a flow rate of 70 mL min^{-1}) as the purge gas. Upon reaching the final temperature, the samples were held for 60 min prior to cooling down to room temperature. The weight of the PAN/PAA fibers was weighed.

4.4. Graphene Wrapping Process. To improve the conductivity and mechanical stability of the electrospun nanofibers, a three-step, graphene wrapping procedure has been adopted from Shin et al.[20] The nanofibers were initially mixed with 50 mL of toluene and 1 mL of APS and refluxed under a nitrogen atmosphere for 24 h (see Figure S1 in the Supporting Information). Functionalization with APS creates positively charged amine groups on the surface of the fibers. The fibers were then rinsed with water in preparation for the next step.

The functionalized fibers were then placed in an aqueous GO solution and stirred for 1 h. The pH of the solution was adjusted to 4 by the addition of hydrochloric acid to maximize the zeta potential difference between the APS-functionalized fibers and GO. Under these conditions, amine groups on the fiber surfaces are protonated (to $-NH_3^+$), and hydroxyl and carboxylic acid groups on GO are ionized (to $-O^-$ and $-COO^-$, respectively). Next, the GO solution was diluted to 0.26 mg mL^{-1}, an optimum condition for the best wrapping conditions.[20]

Finally, 1 mL of hydrazine monohydrate was added to the GO solution to reduce GO. The solution was heated to 80 °C and stirred for 3 h. After heating and stirring, the graphene-wrapped fibers were filtered and cooled to room temperature.

4.5. Scanning Electron Microscopy and Focus Ion Beam Milling. The electrospun PAN/PAA fibers were imaged with a scanning electron microscope (JSM-IT100, JEOL Ltd.) using a 15 kV accelerating voltage. Additionally, fibers were milled and then imaged with dual-beam FIB-SEM (Zeiss Crossbeam 550). Rough milling was carried out at 30 kV with a beam current of 3 nA before polishing using 1.5 nA. SEM images were obtained using drift-compensated frame integration at 2.5 kV using a beam current of 150 pA. The charge compensator was used to reduce charge buildup during imaging.

4.6. Fourier Transform Infrared Spectroscopy. The chemical composition of the graphene-wrapped PAN/PAA fibers was determined by FTIR (Haake Mars 60, Rheonaut). The FTIR spectra were recorded between 4000 and 400 cm^{-1}.

4.7. X-ray Diffraction. Electrospun and carbonized, graphene-wrapped PAN/PAA fibers were characterized using XRD (Bruker D2) with a Cu Kα radiation over an angle ranging from 5 to 50°. GO and rGO are known to have XRD peaks at 11.8 and 25.5°, respectively.[23]

4.8. Raman Spectroscopy. Raman spectroscopy (InVia Raman, Renishaw, UK) was used to conduct molecular analysis of rGO-wrapped fibers. A 785 nm, 300 mW laser was used with a ×50 objective. The exposure time was set at 10 s with a recording range of 500−3200 cm^{-1}. Spectra were baseline-corrected and smoothed using MATLAB.

4.9. Electrochemical Measurements. The electrochemical characteristics of the modified SPCEs were measured by CV using a potentiostat controlled by Nova 2.0 software (Autolab PGSTAT204, Metrohm, Switzerland). Solutions of 2 mM of $K_4Fe(CN)_6$ were prepared in 0.1 M potassium chloride buffer solutions for the CV measurements. Approximately 50 μL of the analyte solution was dropped on top of the sensing area's surface, and CV scans were performed as a function of scan rates (0.02, 0.04, 0.06, 0.08, 0.1, and 0.2 V s^{-1}). The selected voltage window for $K_4Fe(CN)_6$ was −0.4 to +0.8 V.

Additionally, EIS was used to measure the response of the system to an applied sinusoidal perturbation (Autolab PGSTAT204, Metrohm, Switzerland). The conductivity of the nanofibers was determined using the Randles model at room temperature. Measurements were made on all the evaluated variations of the electrode with the 50 μL of 2 mM $K_4Fe(CN)_6$ covering the active area. The procedure for conducting the measurements involved an initial step of measuring the open-circuit potential of the system, which allows enough time for the sample and electrolyte to stabilize and helps the device to determine the fixed DC potential to be held in the following stages. After determining the DC potential component to be held by the cell, the device then proceeds to superpose an AC signal on the system. The signal was fixed at a value of 10 mV_{RMS} and the frequencies probed were selected within the range of 1 Hz to 100 kHz as biological or chemical processes do not entail significant information at frequencies above 100 kHz.[29]

For the work presented here, five types of electrodes were characterized:

1. Bare electrode (SPCE, used as a control);
2. Glue electrode (SPCE with carbon glue, also used as a control);
3. Graphene-wrapped (GW) as-spun nanofiber electrode (nanofibers that have been graphene-wrapped are stuck to the SPCE WE using carbon glue);
4. Carbonized (CB) electrode (nanofibers that have been carbonized are stuck to the SPCE WE using carbon glue);
5. Graphene-wrapped and carbonized (GW + CB) electrode (nanofibers that have been both graphene-wrapped and carbonized are stuck to the SPCE WE using carbon glue).

■ ASSOCIATED CONTENT

Supporting Information

The Supporting Information is available free of charge at https://pubs.acs.org/doi/10.1021/acsomega.0c05823.

Photographs of the graphene wrapping process, FIB-SEM imaging of the graphene-wrapped electrospun fibers, and cyclic voltammograms of electrode samples at 2 and 10 mM $K_4Fe(CN)_6$ (PDF)

■ AUTHOR INFORMATION

Corresponding Author

Norbert Radacsi − *School of Engineering, Institute for Materials and Processes, The University of Edinburgh, Edinburgh EH9 3JL, U.K.;* orcid.org/0000-0002-7358-

https://doi.org/10.1021/acsomega.0c05823
ACS Omega 2021, 6, 10568−10577

951X; Phone: +44 (0) 131 651 7112; Email: n.radacsi@ed.ac.uk

Authors

Andreas Tsiamis − *School of Engineering, Institute for Integrated Micro and Nano Systems, The University of Edinburgh, Edinburgh EH9 3FF, U.K.*

Francisco Diaz Sanchez − *School of Engineering, Institute for Materials and Processes, The University of Edinburgh, Edinburgh EH9 3JL, U.K.*

Niklas Hartikainen − *School of Engineering, Institute for Materials and Processes, The University of Edinburgh, Edinburgh EH9 3JL, U.K.*

Michael Chung − *School of Engineering, Institute for Materials and Processes, The University of Edinburgh, Edinburgh EH9 3JL, U.K.*

Srinjoy Mitra − *School of Engineering, Institute for Integrated Micro and Nano Systems, The University of Edinburgh, Edinburgh EH9 3FF, U.K.*

Ying Chin Lim − *Faculty of Applied Sciences, Universiti Teknologi MARA, 40450 Shah Alam, Selangor, Malaysia*

Huey Ling Tan − *Faculty of Chemical Engineering, Universiti Teknologi MARA, 40450 Shah Alam, Selangor, Malaysia*

Complete contact information is available at: https://pubs.acs.org/10.1021/acsomega.0c05823

Author Contributions

A.T.: data analysis and writing (original draft, review, and editing). F.D.S.: sensor characterization, data analysis, and writing (original draft, review, and editing). N.H.: sensor fabrication and characterization, data analysis, and writing (original draft). M.C.: sensor characterization (Raman), data analysis, and writing (review and editing). S.M.: writing (review and editing) and supervision. Y.C.L.: writing (review and editing). H.L.T.: experiments and writing (review and editing). N.R.: conceptualization, writing (review and editing), and supervision.

Notes

The authors declare no competing financial interest.

■ ACKNOWLEDGMENTS

The authors are grateful to acknowledge the University Teknologi MARA for the funding through grants 600-RMC 5/3/GRR (005/2020) and 600-RMC/GPK 5/3 (153/2020). The authors would like to thank the Castansa Trust for their donation of the scanning electron microscope (JEOL JSM-IT100) used for imaging and also acknowledge the use of the Cryo FIB/SEM (Zeiss Crossbeam 550) bought with EPSRC grant EP/P030564/1. M.C. was supported by the Engineering and Physical Sciences Research Council (EPSRC) Centre for Doctoral Training in Intelligent Sensing and Measurement, grant number EP/L016753/1. The authors would also like to thank Fergus Dingwall for laboratory assistance, Thomas Glen for FIB/SEM image acquisition, and William Skinner for Raman analysis. Finally, the authors would like to thank Muhammad Waqas for assistance with the drawings of the nozzle-free electrospinning setup.

■ REFERENCES

(1) Gao, A.; Lu, N.; Wang, Y.; Li, T. Robust ultrasensitive tunneling-FET biosensor for point-of-care diagnostics. *Sci. Rep.* **2016**, *6*, 22554.

(2) Logothetidis, S. Nanotechnology in Medicine: The Medicine of Tomorrow and Nanomedicine. *Hippokratia* **2006**, *10*, 7−21.

(3) Farokhzad, O. C.; Langer, R. Impact of Nanotechnology on Drug Delivery. *Perspective* **2009**, *3*, 16−20.

(4) Wang, Z.; Wu, S.; Wang, J.; Yu, A.; Wei, G. Carbon Nanofiber-Based Functional Nanomaterials for Sensor Applications. *Nanomaterials* **2019**, *9*, 1045.

(5) Stout, D. Recent Advancements in Carbon Nanofiber and Carbon Nanotube Applications in Drug Delivery and Tissue Engineering. *Curr. Pharm. Des.* **2015**, *21*, 2037−2044.

(6) de Faria, A. F.; Perreault, F.; Shaulsky, E.; Arias Chavez, L. H.; Elimelech, M. Antimicrobial Electrospun Biopolymer Nanofiber Mats Functionalized with Graphene Oxide-Silver Nanocomposites. *ACS Appl. Mater. Interfaces* **2015**, *7*, 12751−12759.

(7) Eivazzadeh-Keihan, R.; et al. Carbon based nanomaterials for tissue engineering of bone: Building new bone on small black scaffolds: A review. *J. Adv. Res.* **2019**, *18*, 185−201.

(8) Zhang, B.; Kang, F.; Tarascon, J.-M.; Kim, J.-K. Recent advances in electrospun carbon nanofibers and their application in electrochemical energy storage. *Prog. Mater. Sci.* **2016**, *76*, 319−380.

(9) Yue, L.; et al. Recent advances in electrospun one-dimensional carbon nanofiber structures/heterostructures as anode materials for sodium ion batteries. *J. Mater. Chem. A* **2020**, *8*, 11493−11510.

(10) Sapountzi, E.; Braiek, M.; Chateaux, J.-F.; Jaffrezic-Renault, N.; Lagarde, F. Recent Advances in Electrospun Nanofiber Interfaces for Biosensing Devices. *Sensors* **2017**, *17*, 1887.

(11) Murthe, S. S.; et al. 11—Electrospun Nanofibers for Biosensing Applications. *Nanobiosensors for Biomolecular Targeting*; Micro and Nano Technologies; Elsevier, 2019, 253−267.

(12) Nie, G.; Zhao, X.; Luan, Y.; Jiang, J.; Kou, Z.; Wang, J. Key issues facing electrospun carbon nanofibers in energy applications: on-going approaches and challenges. *Nanoscale* **2020**, *12*, 13225−13248.

(13) Yang, G.; Li, L.; Lee, W. B.; Ng, M. C. Structure of graphene and its disorders: a review. *Sci. Technol. Adv. Mater.* **2018**, *19*, 613−648.

(14) Lee, C.; Wei, X.; Kysar, J. W.; Hone, J. Measurement of the Elastic Properties and Intrinsic Strength of Monolayer Graphene. *Science* **2008**, *321*, 385−388.

(15) Georgakilas, V.; Tiwari, J. N.; Kemp, K. C.; Perman, J. A.; Bourlinos, A. B.; Kim, K. S.; Zboril, R. Noncovalent Functionalization of Graphene and Graphene Oxide for Energy Materials, Biosensing, Catalytic, and Biomedical Applications. *Chem. Rev.* **2016**, *116*, 5464−5519.

(16) Senthamizhan, A.; Balusamy, B.; Uyar, T. Glucose sensors based on electrospun nanofibers: a review. *Anal. Bioanal. Chem.* **2016**, *408*, 1285−1306.

(17) Smith, A. T.; LaChance, A. M.; Zeng, S.; Liu, B.; Sun, L. Synthesis, properties, and applications of graphene oxide/reduced graphene oxide and their nanocomposites. *Nano Mater. Sci.* **2019**, *1*, 31−47.

(18) Kim, S. Y.; Yang, K. S.; Kim, B.-H. Improving the Microstructure and Electrochemical Performance of Carbon Nanofibers Containing Graphene-Wrapped Silicon Nanoparticles as a Li-Ion Battery Anode. *J. Power Sources* **2015**, *273*, 404−412.

(19) Tan, H. L.; Sanira Putri, M. K.; Idris, S. S.; Hartikainen, N.; Abu Bakar, N. F.; Keirouz, A.; Radacsi, N. "High-throughput fabrication of carbonized electrospun polyacrylonitrile/poly(acrylic acid) nanofibers with additives for enhanced electrochemical sensing. *J. Appl. Polym. Sci.* **2020**, *137*, 49341.

(20) Shin, J.; Park, K.; Ryu, W.-H.; Jung, J.-W.; Kim, I.-D. Graphene wrapping as a protective clamping layer anchored to carbon nano fibers encapsulating Si nanoparticles for a Li-ion battery anode. *Nanoscale* **2014**, *6*, 12718−12726.

(21) Pan, W.; He, X.; Chen, Y. Preparation and characterization of polyacrylonitrile/antimony doped tin oxide composite nanofibers by electrospinning method. *Optoelectron. Adv. Mater., Rapid Commun.* **2010**, *4*, 390−394.

(22) Mani, V.; Periasamy, A. P.; Chen, S.-M. Highly selective amperometric nitrite sensor based on chemically reduced graphene oxide modified electrode. *Electrochem. Commun.* **2012**, *17*, 75−78.

(23) Saleem, H.; Haneef, M.; Abbasi, H. Y. Synthesis Route of Reduced Graphene Oxide Via Thermal Reduction of Chemically Exfoliated Graphene Oxide. *Mater. Chem. Phys.* **2017**, *204*, 1−7.
(24) Ferrari, A. C. "Raman spectroscopy of graphene and graphite: Disorder, electron−phonon coupling, doping and nonadiabatic effects. *Solid State Commun.* **2007**, *143*, 47−57.
(25) Wu, J.-B.; Lin, M.-L.; Cong, X.; Liu, H.-N.; Tan, P.-H. Raman Spectroscopy of Graphene-Based Materials And Its Applications in Related Devices. *Chem. Soc. Rev.* **2018**, *47*, 1822−1873.
(26) Moon, I. K.; Lee, J.; Ruoff, R. S.; Lee, H. Reduced graphene oxide by chemical graphitization. *Nat. Commun.* **2010**, *1*, 73.
(27) Khan, Q. A.; Shaur, A.; Khan, T. A.; Joya, Y. F.; Awan, M. S. Characterization of Reduced Graphene Oxide Produced through a Modified Hoffman Method. *Cogent Chem.* **2017**, *3*, 1298980.
(28) de Pauli, M.; Gomes, A. M. C.; Cavalcante, R. L.; Serpa, R. B.; Reis, C. P. S.; Reis, F. T.; Sartorelli, M. L. Capacitance spectra extracted from EIS by a model-free generalized phase element analysis. *Electrochim. Acta* **2019**, *320*, 134366.
(29) Randviir, E. P.; Banks, C. E. Electrochemical impedance spectroscopy: an overview of bioanalytical applications. *Anal. Methods* **2013**, *5*, 1098−1115.

https://doi.org/10.1021/acsomega.0c05823
ACS Omega 2021, 6, 10568−10577